Received: 8 December 2020 | Revised: 24 May 2021 | Accepted: 24 May 2021 | Published on: 12 July 2021

DOI: 10.1002/qj.4110

Quarterly Journal of the Royal Meteorological Society RMetS

RESEARCH ARTICLE

# Upper-level trajectories in the prototype problem for tropical cyclone intensification

**Shanghong Wang**[1,2] | **Roger K. Smith**[1]

[1]Meteorological Institute, Ludwig Maximilians University of Munich, Munich, Germany

[2]Shanghai Typhoon Institute, China Meteorological Administration, Shanghai, China

**Correspondence**
R. K. Smith, Meteorological Institute, Ludwig-Maximilians University of Munich, Theresienstr. 37, Munich 80333, Germany
Email: roger.smith@lmu.de

**Abstract**

Data from an idealized three-dimensional numerical simulation of tropical cyclone intensification are used to calculate Lagrangian air parcel trajectories emanating from the inflow layer that develops beneath the upper-tropospheric outflow layer. It is found that about half of these trajectories end up in the outflow layer itself. The other half slowly subside to the mid- to upper troposphere, below the outflow layer, and drift slowly outwards as a result of a relatively weak overturning circulation in that region. Calculations show that pseudo-equivalent potential temperature is not approximately conserved along the air parcel trajectories, indicating that the turbulent diffusion of heat and moisture and/or the latent heat changes by freezing or melting along the trajectories is appreciable in the mid- and upper troposphere.

**KEYWORDS**

Hurricane, trajectories, tropical cyclone, typhoon

## 1 | INTRODUCTION

The ability to make in situ observations of the upper-level outflow layer in tropical cyclones using dropsondes released from high-flying aircraft and unmanned drones has led to renewed efforts to understand the role of the outflow layer in tropical cyclone behaviour (e.g., Komaromi and Doyle, 2017, Doyle *et al.*, 2017, Tao *et al.*, 2019, Montgomery *et al.*, 2020, Wang *et al.*, 2020). Two of these observational studies noted that, adjacent to the outflow layer, there are sometimes inflow layers as well (Komaromi and Doyle, 2017, Smith *et al.*, 2019).

For a long time now, dating back at least to the pioneering study of Rotunno and Emanuel (1987), upper-tropospheric inflow layers have been known to develop in numerical model simulations of tropical cyclone intensification when the vertical resolution of the model is sufficiently fine. A list of specific references is given by Wang *et al.* (2020). A recent article by Corsaro and Toumi (2017) showed that the upper-level inflow layers occur also in model simulations on a $\beta$-plane. Nevertheless, to our knowledge, the reasons for the occurrence of the inflow layers and their significance in cyclone behaviour have received little attention. Indeed, they are not considered when treating the tropical cyclone as a type of thermodynamic Carnot heat engine (e.g., Emanuel, 1986; 1988; 1991; 2018 and references therein).

In a recent analysis of the mean and eddy contributions to tropical cyclone spin-up in an idealized, high-resolution, numerical simulation of tropical cyclone intensification, Montgomery *et al.* (2020) proposed that the shallow layers of inflow that typically sandwich the upper-level outflow are driven by a negative agradient force (including eddy effects) that appears to be a response to the presence of the outflow itself. They found that such a force exists throughout most of the upper troposphere beyond a certain radius. That study raised a number of questions concerning the inflow layers and motivated a

more detailed investigation of them. The results of this investigation were reported by Wang *et al.* (2020).

The two idealized numerical modelling studies by Montgomery *et al.* (2020) and Wang *et al.* (2020) focussed on the prototype problem for tropical cyclone intensification, which considers the evolution of a vortex on an $f$-plane in a quiescent environment, starting from an initially symmetric, moist, cloud-free vortex over a warm ocean. In both cases, the numerical model was three dimensional, but that used by Wang *et al.* used increased vertical resolution in the upper troposphere and reduced vertical resolution at low levels to provide a higher vertical resolution than is usual in the upper troposphere. In addition, because of its focus on the upper troposphere, the new simulation included a representation of cloud microphysics, unlike that of Montgomery *et al.* (2020), which adopted a simpler warm-rain representation of moist processes. Despite the inclusion of ice processes in the present calculation and that of Wang *et al.* (2020), radiation effects are not included explicitly, but are modelled by a Newtonion relaxation of the ambient temperature with a relaxation time scale of 10 days. A justification for this procedure is given by Smith *et al.* (2021) (see appendix therein).

The two foregoing studies suggested a new way to think about the inflow layers above and below the outflow layer found in the model simulations. Wang *et al.* showed that, from an azimuthally averaged perspective, the outflow is driven near its source primarily by a positive agradient force in which the sum of the centrifugal and Coriolis forces in the radial direction is partly opposed by the radially inward pressure gradient force. As air parcels move outwards, approximately conserving their absolute angular momentum, their tangential velocity diminishes, whereupon so does the sum of the centrifugal and Coriolis forces. Well beyond the source, the inward-directed radial pressure gradient force ultimately dominates and leads to a deceleration of the outflow. The inward pressure gradient force extends vertically above and below the outflow layer and leads to a flow response on either side of the outflow layer, where it accelerates air parcels inwards. In essence, the analyses support a previous idea of Ooyama (1987) that views the outflow layer as an expanding jet of air emanating from a radial mass and momentum source where the eyewall convection terminates.

Wang *et al.* showed that the inflow layers are more asymmetric than the outflow layer, having a low-azimuthal-wavenumber flow asymmetry. Nevertheless, the region of maximum inflow above and below the outflow layer tends to align with that of maximum outflow, which, to a first approximation, supports the foregoing interpretation of the inflow layers based on axisymmetric reasoning.

Wang *et al.* showed also that an alternative explanation for the inflow layers in terms of axisymmetric balance dynamics is problematic. In fact, their analysis indicated a significant degree of imbalance in the upper troposphere. They showed further that the inflow layers play a role in modifying the vortex structure in the upper troposphere. The inflow layer above the outflow layer leads to a spin-up of the tangential winds there, thereby extending the cyclonic circulation of the hurricane vertically. In addition, the inflow acts to resist the radial spread of air with high equivalent potential temperature at this level. The inflow layer below the outflow layer leads also to a spin-up of the cyclonic tangential winds in the inflow layer and would appear to contribute to an increase of the radial gradient of equivalent potential temperature at the outer edge of the eyewall.

Two unanswered questions about the inflow layer beneath the outflow layer are: Where does this air go, and what is the impact on the thermodynamics of the upper troposphere? The present article addresses these questions by carrying out a series of trajectory calculations and calculating the variation of pseudo-equivalent potential temperature, $\theta_e$, along these trajectories.

The article is organized as follows: Section 2 describes the method for calculating the trajectories and model output used. Section 3 presents the main results of the trajectory calculations, showing a series of sample trajectories (Section 3.1) and the statistics of many trajectories (Section 3.2). Section 3.1 examines also the variation of equivalent potential temperature along trajectories. Section 4 presents a brief discussion of the relationship of the results to those of a recent study. The conclusions are presented in Section 5.

## 2 | METHOD FOR CALCULATING TRAJECTORIES

The trajectories are calculated using output data from the numerical cloud model CM1 (version cm1r19.8) simulation of Wang *et al.* (2020) stored at 15-min intervals. For these calculations, the simulation was extended for a further 30–120 hr. The simulation was carried out in a rectangular domain 3,000 km in the horizontal and 25 km in the vertical. The horizontal grid spacing in the inner part of the domain, 600 km square, is uniform and equal to 1 km. Outside of this domain, the grid spacing is stretched linearly to 12 km near the outer boundary. The vertical grid spacing is 100 m in the first 1 km and 500 m above 16 km to the top of the domain, the same at all horizontal locations. Between 1 and 16 km, the vertical grid spacing is stretched smoothly from 100 to 500 m. For the present calculations, the output data were interpolated to a new fine grid in a region

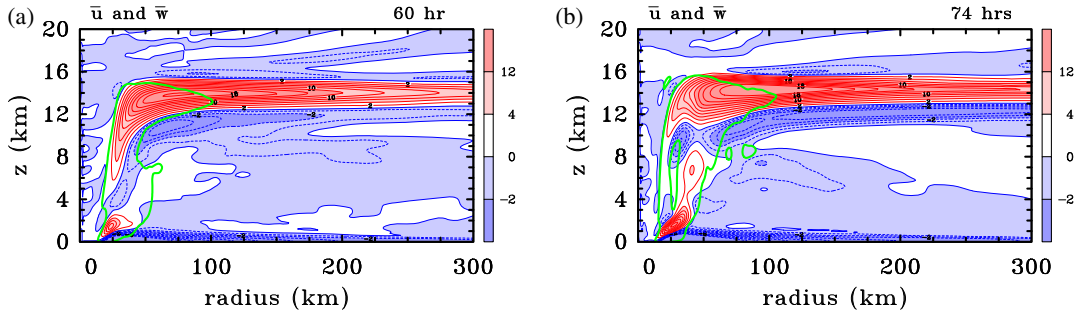


**FIGURE 1** Radius–height cross sections of 1-hr time-averaged (based on 1-min output) and azimuthally averaged radial velocity component, $\bar{u}$, and vertical velocity component, $\overline{w}$, from the numerical model simulation of Wang *et al.*, (2020) at (a) 60 h and (b) 74 h. Contour interval for $\bar{u}$, 2 m·s$^{-1}$ when $\bar{u} > 0$, 1 m·s$^{-1}$ when $\bar{u} < 0$. For $\overline{w}$, the green contours are for $\overline{w} = 0.1$ m·s$^{-1}$. The quantity $\bar{u}$ is shaded with values indicated on the colour bar. Red solid contours indicate positive values; blue dashed contours indicate negative values [Colour figure can be viewed at wileyonlinelibrary.com]

800 km square in the horizontal and 20 km in the vertical using bicubic splines. This new grid has a horizontal grid spacing of 1 km and a vertical grid spacing of 100 m.

For reference, Figure 1 shows the azimuthally averaged radial and vertical velocity fields from the model simulation of Wang *et al.* (2020) at 60 and 74 h. At 60 h (panel (a)), the vortex is near the end of its period of rapid intensification with a maximum azimuthally averaged tangential wind speed of about 60 m·s$^{-1}$ (see Wang *et al.*, 2020, Figure 1a). The inflow layer beneath the upper-level outflow extends to the outer radius shown (300 km) with the maximum inflow at height of about 11 km. At 74 h, which is during the mature phase, the upper-level outflow and the inflow layer beneath have strengthened (panel (b)) and the maximum inflow has risen to about 12 km height.

The main set of trajectory calculations start at 60 h of model integration. These calculations are for air parcels located every 2 km, from 60 km radius to 130 km radius and every 5° in azimuth at height of 11 km, which is within the upper inflow layer beneath the outflow layer (Figure 1). In total, there are 2,592 trajectories for this time. Here, 60 km is chosen as it is the radius where the azimuthally averaged vertical velocity is zero and therefore beyond the eyewall updraught. The 130 km radius is chosen to encompass the extent of relatively strong inflow, being where the azimuthally averaged radial inflow velocity falls below 2 m·s$^{-1}$ in magnitude (Figure 1a). The details of other sets of trajectories are described where they are discussed.

The computation of trajectories uses the formula

$$\vec{r}_{t_{n+1}} = \vec{r}_{t_n} + \frac{1}{2}(\vec{V}_{t_{n+1}} + \vec{V}_{t_n})\Delta t, \qquad (1)$$

where $\vec{r}_{t_n}$ is the three-dimensional position vector of an air parcel at time $t_n$, $\vec{V}_{t_n}$ is the three-dimensional velocity vector at the location of the parcel at this time and $\Delta t$ is the time step, here 15 min. A tri-linear interpolation is used to determine $\vec{V}_{t_n}$ when the air parcel does not lie on a model grid point. If an air parcel moves beyond a radius of 400 km from the vortex centre or above 20 km in height, the calculation for that air parcel is terminated.

## 3 | RESULTS

### 3.1 | Sample trajectories

Figure 2 shows two sets of eight trajectories, each starting along a radial line from 60 km radius to 130 km radius with a spacing of 10 km and having a duration of 24 h. The left column of Figure 2 shows trajectories of air parcels with initial positions along a radial line located in the quadrant with a relatively strong inflow component (see Figure 6c in Wang *et al.*, 2020). The three panels (a), (c) and (e) of Figure 2 provide different perspectives of the trajectories. There are two main groups of trajectories in this set:

1. The air parcels starting at 70, 80 and 110 km radius spiral cyclonically inwards before entering the eyewall updraught. They ascend in the updraught and move rapidly outwards in the outflow layer, taking less than 12 hr to move more than 250 km in radius from the vortex centre.
2. The air parcels starting at 90, 100, 120 and 130 km radius spiral cyclonically inwards before subsiding beyond the eyewall updraught to a layer between about 8 and 9 km, where the radial flow is relatively weak. Subsequently, they move slowly outwards. Even after 24 hr, these air parcels remain within a radius of 250 km from the vortex centre.

Unlike the two types above, the air parcel initialized at 60 km first descends like those in group (2), but it does not descend as far, remaining above 10 km height. Its subsequent motion is erratic in both the horizontal

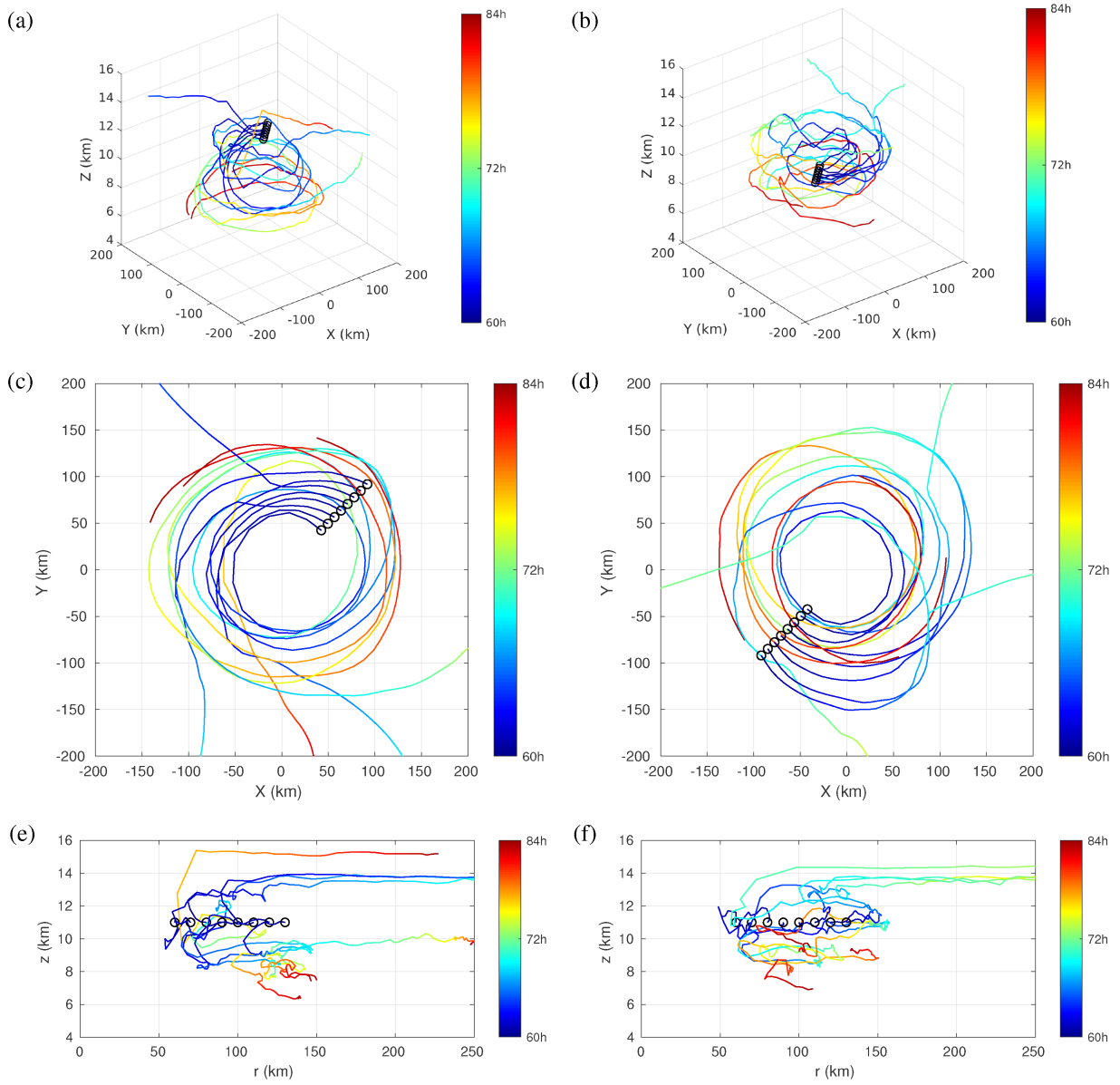


**FIGURE 2** Two sets of eight 24-hr trajectories, each starting along a radial line in the inflow layer below the upper-tropospheric outflow layer at altitude of 11 km. Trajectories in the left column lie in the quadrant with a relatively strong inflow, while those in the right column lie in a quadrant where the inflow is relatively weak. (a) and (b) show a three-dimensional view; (c) and (d) show a horizontal plan view; (e) and (f) show a vertical plan view in the radius–height plane. Initial locations are marked by black circles. Time evolution indicated in the colour bar [Colour figure can be viewed at wileyonlinelibrary.com]

and vertical, at one point rising to 12 km altitude. After about 18 h, this air parcel enters the eyewall updraught, ascending rapidly before entering the outflow and moving outwards like the air parcels in group (1).

The right column of Figure 2 shows trajectories with initial positions along a radial line located in the quadrant with a relatively weak inflow component (see Figure 6c of Wang *et al.*, 2020). As in the previous set of trajectories, the behaviour in this case is not systematic in radius. The air parcels starting at 70, 90 km and further move outwards at first, but turn inwards later. Of these, the parcels starting at 70, 90 and 100 km spiral cyclonically downwards and outwards, ending up after 24 hr in the middle layer. In contrast, the parcels starting at 110 km and beyond spiral upwards in the eyewall updraught and are carried outwards in the outflow layer. The remaining air parcels starting at 60 and 80 km both spiral inwards and downwards at first, but their subsequent tracks differ. The parcel starting at 60 km slowly spirals outwards to the middle layer, while that starting at 80 km enters a strong updraught and ends up in the outflow layer. As in the previous set of trajectories, the air parcels which end

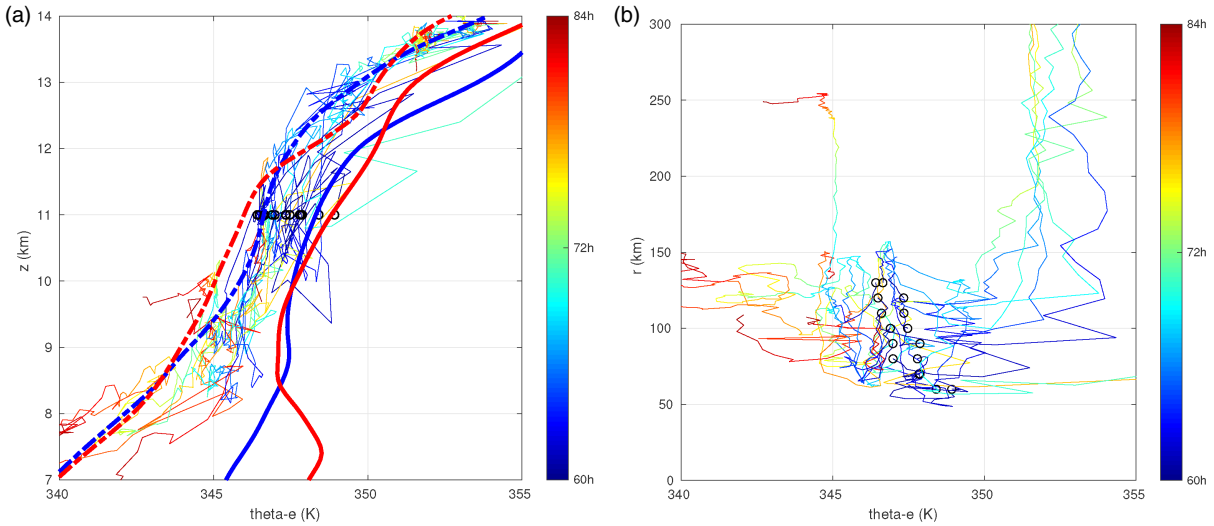


**FIGURE 3** Variations of pseudo-equivalent potential temperature, $\theta_e$, along the 16 trajectories in Figure 2 (thin curves) as a function of height, $z$, in panel (a) and a function of radius, $r$, in panel (b). Curves are colour coded to indicate time as shown on the colour bar. Thick curves in (a) show for reference the azimuthally averaged profiles of $\theta_e$ at a radius of 60 km at 60 hr (blue) and 84 hr (red). Dashed curves show similar reference profiles at 130 km radius [Colour figure can be viewed at wileyonlinelibrary.com]

up in the outflow layer take less than 12 hr to move more than 250 km in radius from the vortex centre, while those that descend to the middle layer remain within a radius of 150 km after 24 hr.

At this point it is worth noting that, although the data used for the trajectory calculations have a relatively high spatial resolution, our available computing facilities did not allow the three-dimensional model data to be stored more frequently than every 15 min[1]. This limitation appears to be most serious in short segments of trajectories where air parcels ascend rapidly in the eyewall updraught. In general, this limitation is not likely to have a significant impact on our findings.

It is clear from the foregoing analysis that, as a result of even low-azimuthal-wavenumber variations in vortex structure, there is a complex 'stirring' taking place within the middle and upper levels of the vortex as a result of the inflow layers. In the absence of turbulent diffusion, this stirring would contribute to a rich structure in the pattern of approximately materially conserved quantities such as pseudo-equivalent potential temperature, $\theta_e$ [2]. In reality, of course, such a structure might be considerably modified by diffusion and to some extent by the latent heat release by freezing. The effects of stirring and diffusion in a simple barotropic vortex flow are discussed by Meunier and Villermaux (2003).

To investigate briefly the effects of the turbulent diffusion of heat and moisture and the latent heat release by freezing on the $\theta_e$-distribution, we show in Figure 3 the values of $\theta_e$ along the tracks of the 16 air parcels investigated in Figure 2. Figure 3a shows the variation of $\theta_e$ as a function of height, $z$. Shown also are the vertical profiles of azimuthally averaged values of $\theta_e$ at radii of 60 and 130 km, the extremes of the initial air parcel locations at the initial time (60 hr) and final time (84 hr) of the trajectory calculations. The profiles at 84 hr are shown merely to judge the temporal variation of the profiles, but, of course, air parcels do not, in general, remain in the annulus between 60 and 130 km radius. If $\theta_e$ were approximately materially conserved, the values of $\theta_e$ along parcel trajectories would be seen as approximately vertical lines in the figure. The fact that this is not the case and that the values lie mostly within the range of values of the azimuthally averaged profiles between 60 and 130 km radius at 60 hr (the thick solid lines in the figure) is strong evidence that turbulent diffusion of heat and moisture and/or latent heat released by freezing along trajectories is appreciable in the mid- and upper troposphere.

A similar result is found by examining the variation of $\theta_e$ as a function of radius, $r$, as shown in Figure 3b. Early on, the $\theta_e$ curves are more horizontal than vertical, again an indication that $\theta_e$ is not approximately materially conserved. At later times, some of the trajectories with high $\theta_e$ appear as approximately vertical lines beyond 150 km radius. These air parcels acquire heat by mixing with higher $\theta_e$ when they enter the eyewall updraught and possibly by latent heat release of freezing as they ascend,

[1]With hindsight, it would have been possible to do trajectory calculations at model runtime, but the decision to carry out these calculations was made at a later stage of the study.

[2]The pseudo-equivalent potential temperature was calculated using the formula given by equation (43) in Bolton (1980).

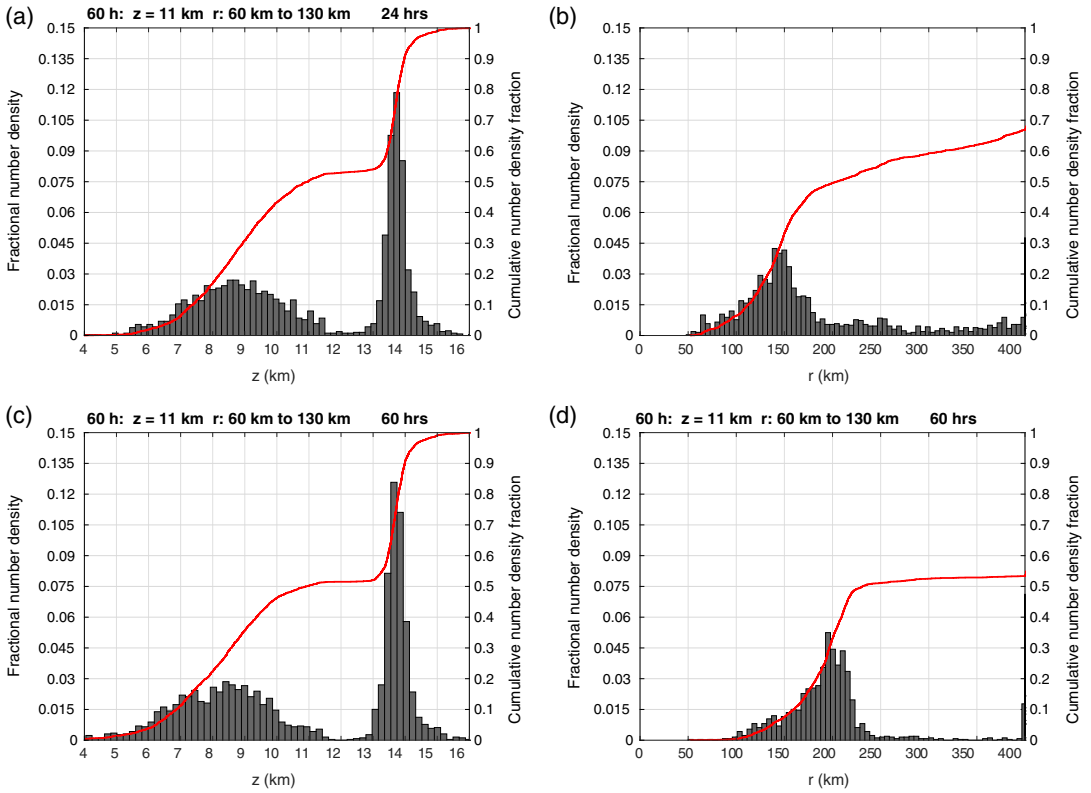


**FIGURE 4** Histograms of end locations of 2,592 trajectories initialized in the inflow layer at 11 km height at 60 hr as described in the text. (a, c) show the height distribution of end locations, (b, d) show the radial distribution of end locations inside a radius of 400 km. Upper panels for 24 hr trajectories, lower panels for 60 hr trajectories. Bin number is 100 for each panel. Number density is expressed as a proportion of the total number of trajectories. The red curves show the cumulative number density fraction [Colour figure can be viewed at wileyonlinelibrary.com]

and they approximately conserve $\theta_e$ as they move outwards in the outflow layer. In contrast, air parcels that descend to the middle layer continue to lose $\theta_e$ by mixing with their new environment and/or by the melting of ice. Despite the fact that this result is dependent in part on the fidelity of the representation of turbulent diffusion in the CM1 model, it would be reasonable to surmise that the same would be true in the real atmosphere.

Further analysis of the effects of diffusion in the mid-/upper troposphere in these simulations would be possible using the isentropic compositing approach of Pauluis and Mrowiec (2013), but this has not been attempted in view of the effort involved in relation to the likely additional insights. Such analyses have been employed in the tropical cyclone context by Mrowiec *et al.* (2016) and Alland *et al.* (2017). It may be interesting to note that upper-tropospheric inflow layers were found in both of these studies, but were not remarked upon.

The implications of the existence of upper-level inflow layers and the inferred strong upper-tropospheric mixing for the thermodynamic Carnot model of tropical cyclones (as reviewed, for example, by Emanuel, 2004) have yet to be determined.

## 3.2 | Statistics of trajectories

The results of the previous section highlight the complexity of trajectories, even when the starting positions are uniformly spaced along a horizontal radial line within the inflow layer. There must be a stochastic element responsible for this complexity because, for example, the rapid ascent of air parcels to the outflow layer takes place in strong and localized deep convective cores, which, themselves, have a stochastic element. Because of this stochastic element, it is appropriate to analyse the statistics of a large number of air parcels starting in the inflow layer. To this end, we examine the distribution of end locations after 24 hr of all 2,592 trajectories calculated in Section 2.

Figure 4a shows a histogram of the heights of the foregoing end locations. Height ranges are divided into 100 bins with the same width, and the number of end trajectories in each bin is divided by the number of trajectories (2,592) to give a fractional number density distribution. The solid red curve in this figure represents the cumulative distribution function. The end trajectories are confined mainly to two layers, one coinciding with the upper outflow layer and the other in the mid- to upper troposphere

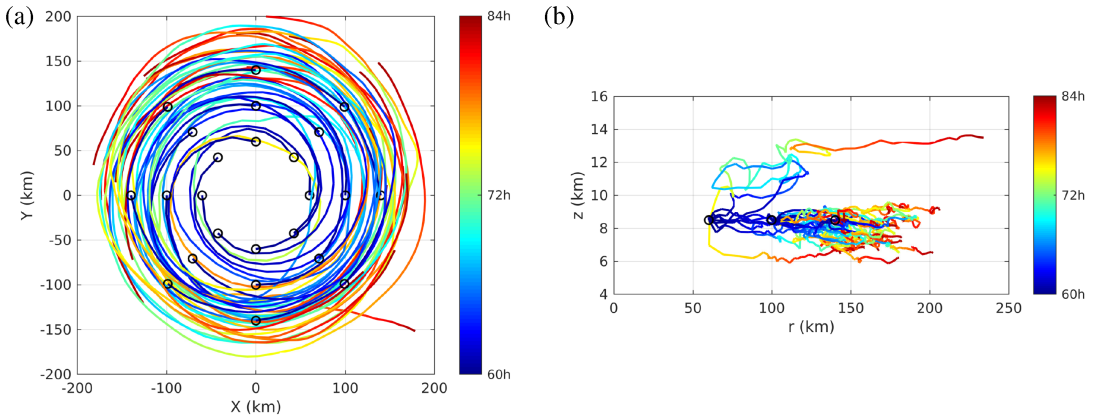


**FIGURE 5** A set of 24, 24-hr trajectories starting at a height of 8.5 km: (a) horizontal plan view; (b) vertical plan view in the radius–height plane. Initial locations are marked by black circles. Time evolution indicated in the colour bar [Colour figure can be viewed at wileyonlinelibrary.com]

somewhat below the outflow layer. The distribution in the outflow layer is relatively sharp with the peak number density at an altitude of about 13.5 km. The distribution in the mid- to upper troposphere is rather broader with a maximum number density at about 8.5 km. The cumulative number density fraction curve shows that air parcels subsiding from the upper inflow layer do not descend below about 5 km. Thus, they do not reach the frictional boundary layer.

Figure 4b shows a histogram similar to that in panel (a) but for the end radii of trajectories after 24 hr. There is a peak of number density at about 150 km, with most trajectories ending up at this radius. All trajectories end up beyond a radius of 50 km, and the distribution has a considerable radial spread with a peak near 150 km radius and a long tail with low number density beyond about 180 km radius. About 33% of trajectories move out beyond a radius of 400 km, which accounts for the reduction of the maximum cumulative number density fraction in the histogram. It turns out that trajectories which descend to the middle layer end within 270 km of the axis, and all those that end beyond this radius ascend to the outflow layer. We have verified this finding by plotting the histogram for only air parcels that descend and only air parcels that ascend (not shown).

Figures 4(c) and (d) show histograms similar to those in panels (a) and (b), but for trajectories of 60 hr duration. The major features of the histogram in panel (c) are essentially the same as those in panel (a). The trajectory end locations show two separate bell-shaped distributions: a broader one with smaller peak value centred near an altitude of 8.5 km and a more peaked one with much larger amplitude near an altitude of 13.8 km. Even the magnitude and spread of these distributions are similar. The intersection of the cumulative number density curve with the reference line at 11 km altitude is 0.5 in both panels, indicating that, at both end times, about half of the trajectories ascend into the outflow while the other half subside. The small differences between the distributions in panels (a) and (c) provide confidence in the robustness of the distributions.

The histogram in Figure 4d shows the radius of the end of trajectories at 60 hr, which should be compared with the situation at 24 hr in Figure 4b. Three features stand out: (a) the peak in the distribution has moved outwards in radius from about 140 km to near 200 km, (b) there are fewer end trajectories beyond about 240 km and (c) the maximum cumulative number density has reduced further to about 53%. The reason for both (b) and (c) is that the end trajectories at larger radii at 24 hr are mostly in the upper level outflow, and by 60 hr, these have moved out of the 400 km domain and are no longer counted. The outward shift in the distribution of end radii is because these trajectories lie in a region of the mid- to upper troposphere where there is a slow outward drift.

If a significant fraction of air parcels in the inflow layer beneath the outflow descend and move slowly outwards at levels mostly between 6 and 10 km, one may ask where the air parcels originally (at 60 hr) move to. To answer this question, we calculate an additional set of 24 air parcel trajectories to those described in Section 2. The air parcels are located initially along radial lines at a height of 8.5 km at 60 hr. The lines are every 45°, and the air parcels are located at 60, 100 and 140 km radius along these lines. The trajectories, which have a duration of 24 hr, are shown in Figure 5.

The majority of these air parcels spiral slowly cyclonically outwards while slowly subsiding. They remain within a radius of 200 km from the vortex centre and above 6 km, even after 24 hr. Evidently, the overturning circulation in the mid- to upper troposphere below the inflow layer and outside the eyewall is relatively weak. Only two air parcels,

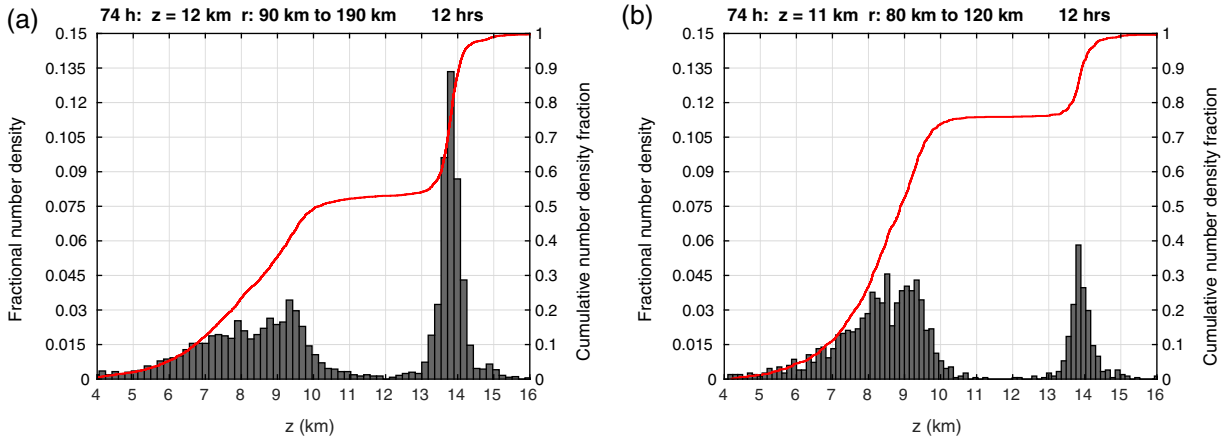


**FIGURE 6** Histograms of height of end locations of (a) 4,032 trajectories initialized in the inflow layer at 12 km height at 74 hr; (b) 4,032 trajectories initialized in the inflow layer at 11 km height at 74 hr; 12 h trajectories are shown. Bin number is 100 for each panel. Number density is expressed as a proportion of the total number of trajectories. The red curves show the cumulative number density fraction [Colour figure can be viewed at wileyonlinelibrary.com]

both initially at 60 km radius, show a different behaviour. They enter a strong updraught area beyond the eyewall in the first 3 hr and are carried into the upper inflow layer at a radius of about 110 km. Then, they spiral cyclonically inwards. One of these air parcels subsequently ascends in the eyewall updraught and moves rapidly outwards in the outflow layer, while the other subsides to about 8 km height.

To judge the representativeness of the above results, histograms of the statistics of two sets of trajectory calculations at 74 hr are shown in Figure 6. Figure 6a shows a histogram of the height of end locations of 4,032 trajectories initialized in the inflow layer at 74 h after 12 hr. Those trajectories are calculated for air parcels located every 2 km from 90 km radius to 190 km radius and every 5° in azimuth at a height of 12 km in the upper inflow layer (Figure 1b). Here, 90 km is chosen as it is the radius where, again, the azimuthally averaged vertical velocity is zero and therefore beyond the eyewall updraught (Figure 1b). As in Figures 4a,c, the distribution of trajectory end heights has two peaks, one in the upper outflow layer and the other in the mid- to upper troposphere. The cumulative number density curve at 12 km shows that about 53% trajectories subside while 47% trajectories ascend into the outflow, comparable to the proportions in Figure 4.

Figure 6b shows a histogram of the end heights of a second set of 1,512 trajectories initialized again in the inflow layer, but at a height of 11 km at 74 hr (cf. Figure 1b). These trajectories are calculated for air parcels located every 2 km from 80 km radius to 120 km radius and every 5° in azimuth in the bottom of the upper inflow layer at a height of 11 km and again end after 12 hr. Once more, 80 km is chosen as it is the radius where the azimuthally averaged vertical velocity is zero. The 120 km radius is chosen to encompass the extent of relatively strong inflow, being where the azimuthally averaged radial inflow velocity falls below 2 $m \cdot s^{-1}$ in magnitude (Figure 1b). It is seen that about 76% of these trajectories subside into the mid- to upper troposphere while only 24% ascend in the eyewall to the outflow layer, presumably because of increased upper-level subsidence at later times as seen in Figure 1b.

## 4 | RELATIONSHIP TO OTHER STUDIES

A much earlier study of trajectories in hurricanes is that of Cram *et al.* (2007), who investigated transport and mixing characteristics of a large sample of air parcels within a high-resolution (2-km horizontal grid spacing) numerical simulation of hurricane Bonnie (1998). The main focus of their article was on the eye, eyewall and nearby environment during the mature stage of this vertically sheared hurricane, but a few back-trajectories were calculated also. These back-trajectories show that one-fifth of the mass in the eyewall at a height of 5 km has an origin in the mid- to upper-level environment. In their Figure 16c, Cram *et al.* show some trajectories at upper levels outside the eyewall updraught that descend along a slanted path to middle levels, similar to the air parcels in group (2) described in Section 3.1.

A more recent article is that by Cohen and Paldor (2020). Whereas our trajectory calculations are based on a three-dimensional numerical simulation and focus on trajectories that start within the inflow layer below the outflow layer, Cohen and Paldor consider only trajectories in the outflow layer within an axisymmetric configuration.

Moreover, they prescribe the pressure gradient in this layer. In general, one cannot do this, of course, because, as noted by Wang *et al.* (2020, see their page 3475), the pressure gradient has to produce accelerations and hence velocities that satisfy mass continuity. For example, in an incompressible (or anelastic) fluid flow, the pressure field is determined diagnostically at any instant of time via a Poisson-type equation by the velocity field in such a way that suitable boundary conditions are satisfied on the flow domain and mass continuity is ensured. For a field of air parcels moving in a prescribed pressure field, the mass continuity constraint must, in general, be forfeited. On these grounds, we have reservations about the results of the Cohen and Paldor study.

## 5 | CONCLUSIONS

This article complements the recent studies by Montgomery *et al.* (2020) and Wang *et al.* (2020) of upper-tropospheric inflow layers commonly found in idealized simulations of tropical cyclone intensification. Data from an idealized and relatively high-resolution three-dimensional numerical simulation are used to investigate the trajectories of air parcels starting in the upper-tropospheric inflow layer just beneath the outflow layer. We show that about half the inflowing air parcels enter the eyewall updraught, where they ascend and are rapidly carried outwards in the outflow layer itself. The remaining air parcels subside and drift slowly outwards in the mid- to upper troposphere, where there is a weak overturning circulation.

A histogram of the distribution of 24 and 60 hr end locations of trajectories shows two peaks in the height: a sharp peak centred at 13.5 km within the upper-level outflow and a broader peak centred at 8.5 km below the inflow layer. The air parcels subsiding from the inflow layer do not descend below about 5 km. The small differences between the distributions for 24 hr trajectories and 60 hr trajectories are an indication of the robustness of these features.

Calculations of pseudo-equivalent potential temperature along the air parcel trajectories indicate that this quantity is not materially conserved, even approximately, indicating that the turbulent diffusion of heat and moisture and/or the latent heat changes by freezing or melting along the trajectories is appreciable in the mid- and upper troposphere. Of course, an extension of this result to the real atmosphere relies in part on the fidelity of the representation of turbulent diffusion in the CM1 model used for the simulation. Nevertheless, the strong diffusion of heat and moisture would mitigate the impact of the inflow layers on the thermodynamics of the upper troposphere compared with the situation if pseudo-equivalent potential temperature were approximately materially conserved. The implications of this strong diffusion and the possible effects of ice, together with the existence of the inflow layers themselves, for the thermodynamic Carnot heat engine model of a mature tropical cyclone have yet to be determined.

While the data available for the foregoing trajectory calculations have relatively high spatial resolution, storage issues restricted the temporal availability of data to 15-min intervals. The limitation appeared most serious in short segments of those trajectories where air parcels ascend rapidly in the eyewall updraught but is unlikely to have a major impact on our findings.

The upper-level inflow layers investigated here may be an important element of the way in which tropical cyclones interact with their environment.

## ACKNOWLEDGEMENTS

We thank Gerard Kilroy for advice in generating the simulation data used for this study, and we thank him, Mike Montgomery and two anonymous reviewers for their perceptive comments on the manuscript. S.W. acknowledges a Ph.D. stipend from the China Scholarship Council.

## ORCID

*Shanghong Wang* https://orcid.org/0000-0002-0773-3448

*Roger K. Smith* https://orcid.org/0000-0002-3668-1608

## REFERENCES

Alland, J.J., Tang, B.H. and Corbosiero, K.L. (2017) Effects of midlevel dry air on development of the axisymmetric tropical cyclone secondary circulation. *Journal of the Atmospheric Sciences*, 74, 1455–1470.

Bolton, D. (1980) The computation of equivalent potential temperature. *Monthly Weather Review*, 108, 1046–1053.

Cohen, Y. and Paldor, N. (2020) Lagrangian trajectories at the outflow of tropical cyclones. *Quarterly Journal of the Royal Meteorological Society*, 147, 58–73.

Corsaro, C.M. and Toumi, R. (2017) A self-weakening mechanism for tropical cyclones. *Quarterly Journal of the Royal Meteorological Society*, 143, 2585–2599.

Cram, T.A., Persing, J., Montgomery, M.T. and Braun, S.A. (2007) A Lagrangian trajectory view on transport and mixing processes between the eye, eyewall, and environment using a high-resolution simulation of Hurricane Bonnie (1998). *Journal of the Atmospheric Sciences*, 64, 1835–1856.

Doyle, J.D., Moskaitis, J.R., Feldmeier, J.W., Ferek, R.J., Beaubien, M., Bell, M.M., Cecil, D.L., Creasey, R.L., Duran, P., Elsberry, R.L., Komaromi, W.A., Molinari, J., Ryglicki, D.R., Stern, D.P., Velden, C.S., Wang, X., Allen, T., Barrett, B.S., Black, P.G., Dunion, J.P., Emanuel, K.A., Harr, P.A., Harrison, L., Hendricks, E.A., Herndon, D., Jeffries, W.Q., Majumdar, S.J., Moore, J.A., Pu, Z., Rogers, R.F., Sanabia, E.R., Tripoli, G.J. and Zhang, D.-L. (2017) A view of tropical cyclones from above: The tropical cyclone intensity

experiment. *Bulletin of the American Meteorological Society*, 98, 2113–2134.

Emanuel, K.A. (1986) An air-sea interaction theory for tropical cyclones. Part I: Steady state maintenance. *Journal of the Atmospheric Sciences*, 43, 585–604.

Emanuel, K.A. (1988) The maximum intensity of hurricanes. *Journal of the Atmospheric Sciences*, 45, 1143–1155.

Emanuel, K.A. (1991) The theory of hurricanes. *Annual Review of Fluid Mechanics*, 23, 179–196.

Emanuel, K.A. (2004). Tropical cyclone energetics and structure. In E. Fedorovich, R. Rotunno, and B. Stevens (Eds.), *Atmospheric Turbulence and Mesoscale Meteorology: Scientific Research Inspired by Doug Lilly*, pp. 165–192: New York: Cambridge University Press.

Emanuel, K.A. (2018) 100 years of progress in tropical cyclone research. *Meteorological Monographs*, 59, 15.1–15.68.

Komaromi, W.A. and Doyle, J.D. (2017) Tropical cyclone outflow and warm core structure as revealed by HS3 dropsonde data. *Monthly Weather Review*, 145, 1339–1359.

Meunier, P. and Villermaux, E. (2003) How vortices mix. *Journal of Fluid Mechanics*, 476, 213–222.

Montgomery, M.T., Kilroy, G., Smith, R.K. and Črnivec, N. (2020) Contribution of eddy momentum processes to tropical cyclone intensification. *Quarterly Journal of the Royal Meteorological Society*, 146, 3101–3117.

Mrowiec, A.A., Pauluis, O.M. and Zhang, F. (2016) Isentropic analysis of a simulated hurricane. *Journal of the Atmospheric Sciences*, 73, 1857–1870.

Ooyama, K.V. (1987). Numerical experiments of steady and transient jets with simple model of the hurricane outflow layer. In:. Preprint, 17th Conference on Hurricanes and Tropical Meteorology. Miami, Florida, American Meteorological Society.

Pauluis, O.M. and Mrowiec, A.A. (2013) Isentropic analysis of convective motions. *Journal of the Atmospheric Sciences*, 70, 3673–3688.

Rotunno, R. and Emanuel, K.A. (1987) An air-sea interaction theory for tropical cyclones. Part II :Evolutionary study using a nonhydrostatic axisymmetric numerical model. *Journal of the Atmospheric Sciences*, 44, 542–561.

Smith, R.K., K. G. and M. T. Montgomery (2021) Tropical cyclone life cycle in a three-dimensional numerical simulation. *Quarterly Journal of the Royal Meteorological Society*, 0, 0–0.

Smith, R.K., Montgomery, M.T. and Braun, S.A. (2019) Azimuthally averaged structure of Hurricane Edouard (2014) just after peak intensity. *Quarterly Journal of the Royal Meteorological Society*, 145, 211–216.

Tao, D., Emanuel, K.A., Zhang, F., Rotunno, R., Bell, M.M. and Nystrom, R.G. (2019) Evaluation of the assumptions in the steady-state tropical cyclone self-stratified outflow using three-dimensional convection-allowing simulations. *Journal of the Atmospheric Sciences*, 76, 2995–3009.

Wang, S., Smith, R.K. and Montgomery, M.T. (2020) Upper-tropospheric inflow layers in tropical cyclones. *Quarterly Journal of the Royal Meteorological Society*, 146, 3466–3487.

**How to cite this article:** Wang, S. & Smith, R.K. (2021) Upper-level trajectories in the prototype problem for tropical cyclone intensification. *Quarterly Journal of the Royal Meteorological Society*, 147(738), 2978–2987. Available from: https://doi.org/10.1002/qj.4110